

Journal of Biomedical Optics

SPIEDigitalLibrary.org/jbo

Time course and topographic distribution of ocular fundus pulsation measured by low-coherence tissue interferometry

Nikolaus Dragostinoff
René M. Werkmeister
József Klaizer
Martin Gröschl
Leopold Schmetterer

Time course and topographic distribution of ocular fundus pulsation measured by low-coherence tissue interferometry

Nikolaus Dragostinoff,^{a,b} René M. Werkmeister,^a József Klaizer,^c Martin Gröschl,^c and Leopold Schmetterer^{a,d}

^aMedical University of Vienna, Center for Medical Physics and Biomedical Engineering, Währinger Gürtel 18-20, Vienna 1090, Austria

^bIntegrated Microsystems Austria GmbH, Viktor Kaplan-Strasse 2/1, Wiener Neustadt 2700, Austria

^cVienna University of Technology, Institut für Angewandte Physik, Wiedner Hauptstrasse 8-10/134, Vienna 1040, Austria

^dMedical University of Vienna, Department of Clinical Pharmacology, Währinger Gürtel 18-20, Vienna 1090, Austria

Abstract. Low-coherence tissue interferometry is a technique for the depth-resolved measurement of ocular fundus pulsations. Whereas fundus pulsation amplitudes at preselected axial positions can readily be assessed by this method, coupling of the interferometer with a pulse oximeter additionally allows for the reconstruction of the time course of ocular fundus pulsation with respect to the cardiac cycle of the subject. For this purpose, the interferogram resulting from the superposition of waves reflected at the cornea and the ocular fundus is recorded synchronously with the plethysmogram. A new method for evaluating the time course of synthetic interferograms in combination with plethysmograms based on averaging several pulse periods has been developed. This technique allows for the analysis of amplitudes, time courses, and phase differences of fundus pulsations at preselected axial and transversal positions and for creating fundus pulsation movies. Measurements are performed in three healthy emmetropic subjects at angles from 0 deg to 18 deg to the axis of vision. Considerably different time courses, amplitudes, and phases with respect to the cardiac cycle are found at different angles. Data on ocular fundus pulsation obtained with this technique can—among other applications—be used to verify and to improve biomechanical models of the eye. © 2013 Society of Photo-Optical Instrumentation Engineers (SPIE) [DOI: 10.1117/1.JBO.18.12.121502]

Keywords: fundus pulsation; ocular tissue movement; low-coherence tissue interferometry.

Paper 130368SSR received May 24, 2013; revised manuscript received Jul. 25, 2013; accepted for publication Aug. 9, 2013; published online Oct. 3, 2013.

1 Introduction

Measurements of heart rate-related distance variations between cornea and retina based on a laser interferometric method have been used for the study of various ocular diseases that are associated with alterations in choroidal blood flow.¹⁻⁶ The distance variations (often referred to as fundus pulsations) are mainly caused by the rhythmic filling of the choroid during the cardiac cycle. During systole, the blood flow entering the eye through the ophthalmic artery exceeds the blood flow leaving the eye through the ocular veins, which leads to a slight protrusion of the retinal structures toward the cornea. Schmetterer et al. have shown that there is a high degree of correlation between the amplitude of the intraocular pressure (IOP) change during the cardiac cycle and the fundus pulsation amplitude (FPA) in healthy young emmetropic subjects.^{5,7,8} They also found an association between FPA and the pulsatile ocular blood flow as calculated from the time course of the IOP changes.^{5,7,8}

The technique employed by Schmetterer et al. uses a laser beam of long coherence length for the illumination of the eye.⁹ The beam is partially reflected at the front surface of the cornea and at several structures within the posterior pole of the eye. The reflections from the cornea generate a wavefront that is nearly spherical, while the reflections from the fundus approximately form a plane wave. Interference of these two

wavefronts generates concentric circular interference fringes, which are observed with a linear CCD array. The time course of the interference pattern yields information about the pulsatile distance changes between cornea and retina. With this technique, however, only the interference pattern with the highest contrast, i.e., the pattern that arises from the waves reflected at the cornea and the strongest reflecting structure at the ocular fundus, can be observed. No information about the depth (position along the optical axis) is contained within the interference pattern, and the movement of structures with lower reflectivity cannot be assessed.

To overcome this problem, low-coherence tissue interferometry (LCTI) has recently been developed by Dragostinoff et al.¹⁰ This technique uses light of low temporal coherence and includes axial eye length measurement. The light emitted by a superluminescent diode (SLD) is split by an external Michelson interferometer into two components. By putting the interferometer arms at different lengths, a path length difference is introduced that equals twice the arm length difference. The two components are guided onto the eye and are, as described earlier, reflected at the cornea and at the fundus. Because of the low coherence length of the light, interference patterns will occur only when the optical path difference between the cornea and a structure within the posterior pole of the eye equals (within the coherence length) the arm length difference of the Michelson interferometer. Thus, in the first measurement step, the axial positions of reflecting structures

Address all correspondence to: Leopold Schmetterer, Medical University of Vienna, Center for Medical Physics and Biomedical Engineering, Währinger Gürtel 18-20, Vienna 1090, Austria. Tel: +431404002981; Fax: +431404002998; E-mail: leopold.schmetterer@meduniwien.ac.at

within the fundus are obtained by moving the stepping motor and by measuring the intensity of the interference pattern similar to low-coherence interferometry, which results in a depth profile (A-scan) at the desired sample location.^{11,12} In the second step, an intensity peak corresponding to a reflecting structure is selected, and the stepping motor is moved to the position of the peak. The interference pattern is then imaged onto a linear CCD array and recorded over time, resulting in a so-called synthetic interferogram covering information about the distance change between the cornea and the selected structure within the fundus. Thus, LCTI enables measuring the movement of structures in preselected, well-defined depths and comparing fundus pulsations at different axial positions.

LCTI can provide much-needed data for both verification and improvement of biomechanical models of the eye; in particular about the influence of IOP on the forces of the optic nerve head (ONH). Biomechanical properties of the ONH are, beside vascular factors,^{13–15} hypothesized to play an important role in the development and progression of glaucoma.^{16,17} Models of ONH biomechanics at different levels of complexity have been proposed in recent years.^{18–24} However, current biomechanical models use data from *in vitro* or *ex vivo* measurements for the determination of the mechanical parameters. With LCTI, the response of ocular tissue in different depths to the changes in IOP during the cardiac cycle can be measured, which can be used for the determination of material properties of the respective tissue. Further, the pulsatile movement of the ocular structures, as measured by LCTI, can be compared with predictions of biomechanical models and can be used for refinement of the models.

2 Principles of Pulse-Correlated LCTI

The principles and optical setup of LCTI are described in detail in Ref. 10. In the following, only a brief overview of LCTI is given.

As a first step in LCTI, the optical distance between the anterior surface of the cornea and the reflecting layers at the ocular fundus is measured. This axial eye length measurement is based on dual-beam partial coherence interferometry (dual-beam PCI). In this technique, light of high spatial coherence but low temporal coherence is used for the illumination of the sample. The light from a SLD with coherence length l_c is split by a Michelson interferometer into two components with path length difference d . These two beam components are guided onto the eye and reflected at the cornea and the various structures in the fundus. If one of the intraocular distances matches (within l_c) the path difference d , interference of the reflected beam components is observed. Depth ranging is provided by one of the interferometer mirrors, which is mounted on a stepping motor and moved at constant speed over a certain distance. The light reflected from the subject's eye is focused onto an avalanche photo diode (APD). The signal from the APD is amplified and filtered, which results in a one-dimensional depth-resolved cross-section of the sample called optical A-scan. From the positions of the signal peaks in an A-scan, the respective intraocular distances can be obtained. The advantage of dual-beam PCI over conventional PCI is the elimination of longitudinal eye motions, since the distances are measured relative to the anterior corneal surface.

In the second measurement step, one of the peaks corresponding to a reflecting structure is selected, and the stepping motor is moved to that position. Since the arm length difference

of the Michelson interferometer now equals the optical distance between the front surface of the cornea and the selected structure, an interference pattern can be observed. As mentioned earlier, the wave originating from the cornea is close to spherical, while the reflection from the fundus approximately forms a plane wave. Thus, the interference pattern consists of nonlocalized concentric circular fringes with a maximum contrast in a distance of 30 to 40 mm in front of the eye. The plane of maximum contrast is imaged onto a linear CCD array connected to a PC, which records the signal over time resulting in a synthetic interferogram. A distance variation between the cornea and the preselected structure in the fundus induces a change in interference order $\Delta N(t)$, which can be determined from the synthetic interferogram by counting the fringes moving through a fixed point. The optical distance change $\Delta L(t)$ can be calculated by $\Delta L(t) = \Delta N(t) * \lambda/2$, where λ is the central wavelength of the light source. This equation allows for the calculation of the time course of the fundus pulsation and the respective FPA.

With the described method, the time course of movements of ocular tissue structures can be determined in preselected depths and (using an internal fixation target) preselected angles to the axis of vision. However, for determining the phase difference between the fundus pulsation and the cardiac cycle, more information than is contained in a synthetic interferogram is needed. For this purpose, we used a pulse oximeter with a finger-clip sensor to record the plethysmograms of the subjects under study alongside with the synthetic interferograms. For reconstruction of the time courses of the movements with respect to the heart cycle, we developed a new method based on averaging multiple pulse periods. With this technique, the phases of fundus pulsations in different depths and at different angles to the axis of vision can be compared. Furthermore, fundus pulsation movies can be created from the reconstructed time courses.

3 Methods

3.1 System Overview

As light source, an SLD from Superlum (Cork, Ireland) with a central wavelength λ of 840 nm and a coherence length l_c of 11.6 μm (in air) was used. l_c is considerably larger than typical FPAs (2 to 8 μm), which allows the observation of changes in the interference pattern induced by fundus pulsations as long as the stepping motor is in a position corresponding to the measured tissue structure. For the observation of the interference pattern, the plane of highest fringe contrast was imaged onto a CCD line camera (ILX 551, 2048 pixels, 14 \times 14- μm pixel size, 8-bit resolution from Sony, Tokyo, Japan) that was positioned in the center of the interference fringes and operated at a line readout rate of 600 Hz. For more details on the optical setup, we refer to our previous publication.¹⁰ A green light-emitting diode (LED), which was collimated with a lens ($f = 30$ mm) and coupled into the system by a pellicle beamsplitter (8R/92T) directly before the measured eye, was used as fixation target.

Plethysmograms were recorded using a pulse oximeter (ChipOx Development Kit with finger-clip sensor from CorScience GmbH, Erlangen, Germany), connected to the PC via RS232 and read-out simultaneously with the CCD camera (see Fig. 1). The topmost image in Fig. 1 shows a synthetic interferogram recorded *in vivo* at a preselected axial depth, containing information on the time course of the distance change

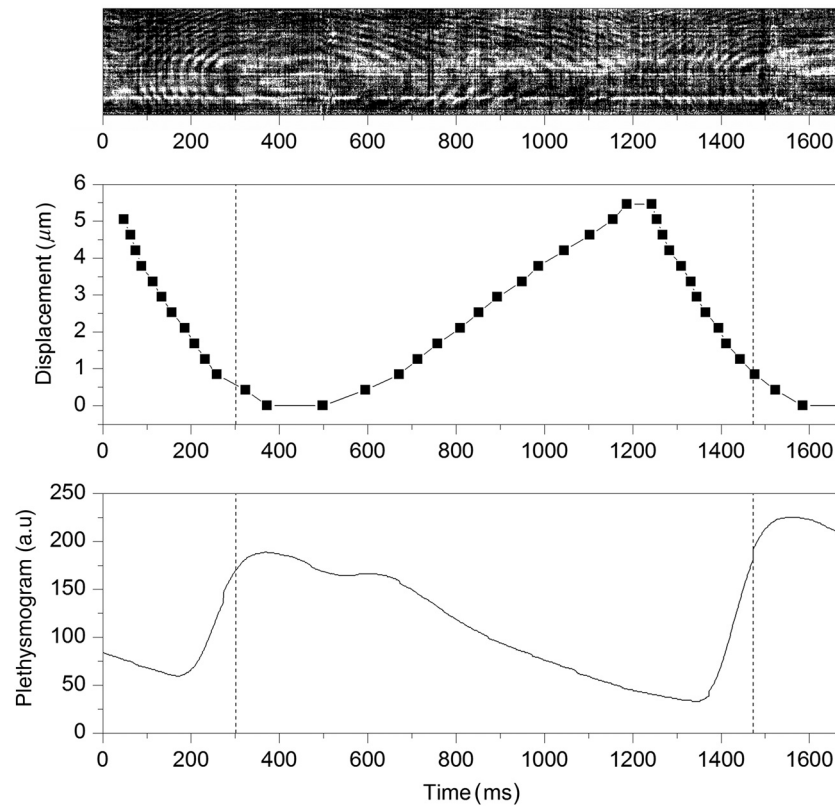


Fig. 1 Synthetic interferogram recorded *in vivo* at a frequency of 600 Hz and at an angle of 12 deg nasal to the axis of vision from a healthy young subject (subject 1, axial position 31.315 mm) together with contraction-dilatation graph and plethysmogram. Pulse periods are marked by vertical dashed lines.

between the cornea and the selected fundus layer. In this image, the horizontal axis represents the time, while the vertical axis corresponds to the intensity distribution on the linear CCD array. Thus, the image shows the time course of the intensity of a linear section in the center of the interference fringes. Each opening (i.e., new) interference fringe corresponds to a change in interference order ΔN of -1 , while ΔN increases by $+1$ for each closing (disappearing) interference fringe. The fringe counting method and the resulting time course of contraction and dilatation, in the following referred to as displacement, are demonstrated by the graph in the middle, where the horizontal axis again represents the time and the vertical axis represents the distance change between the ocular layers. The signal recorded from the finger-clip sensor over time (plethysmogram) is shown in the bottom graph.

3.2 Data Analysis

Usually, 10 to 40 interference fringes occur during each pulse period, corresponding to an FPA range of approximately 2 to 8 μm . Note that only half of the fringes account for the FPA, since the pulse cycle contains both contraction and dilatation, e.g., a pulse period containing 10 fringes (five opening and five closing fringes) corresponds to an FPA of $\Delta N * \lambda / 2 = 5 * 0.84 / 2 = 2.1 \mu\text{m}$. Low FPAs are measured in the region of the macula, while the highest FPAs occur in the ONH. From Fig. 1, it can be seen that the contraction-dilatation graph is not smooth, due to the relatively small number of fringes. Additionally, the FPA can be influenced by fringe counting errors (fringes that are missed or counted twice

because of intensity fluctuations). For obtaining smooth time courses and more accurate FPAs, multiple pulse periods need to be averaged. However, averaging of different pulse cycles is difficult because of the slightly different durations of the pulses (fluctuations in cardiac cycle) and missing fringes (due to blinking, eye movements, etc.) in some cycles. To overcome these problems, a new method for the averaging of different pulse periods was developed.

As a first step of data evaluation, the plethysmogram is split into single-pulse cycles. For this purpose, each plethysmogram position where the value passes 80% of the subsequent local maximum is marked so that the plethysmogram and synthetic interferogram can be split into sections that lie between these marks. In the next step, each pulse cycle is divided into 100 equally distributed parts, which in the end allows for averaging cycles of different durations. Figure 2 exemplarily shows the change in interference order over time in three different pulse cycles, where each pulse cycle is split up into parts numbered 1...100. Each interference fringe in the synthetic interferogram is manually assigned an interference order N , beginning with $N = 0$ at the innermost (usually closed) fringe, i.e., the last fringe of the systole and the first fringe of the diastole. The adjacent fringes to the left and the right are assigned $N = 1$, and so forth. Linear interpolation of the interference orders is performed between all marked fringes, so that an N value can be assigned to as many of the 100 parts of the pulse cycle as possible (see Fig. 2). Only the parts that lie before the first and after the last marked interference fringes are not assigned an interference order with this method. Marking of interference fringes is performed for several pulse periods, where interference fringes

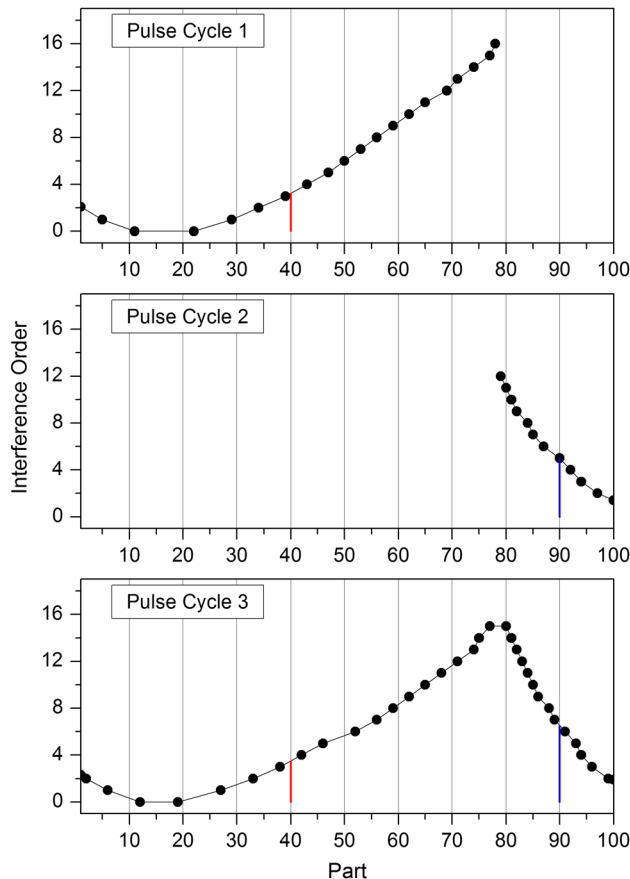


Fig. 2 Change in interference order over time in three pulse cycles. Each pulse cycle is split up into 100 parts, and linear interpolation is performed between data points obtained by marking of interference fringes in the synthetic interferogram. Red and blue lines indicate parts where pulse cycles 1 and 3 (red) and pulse cycles 2 and 3 (blue) contribute to the averaging process (see text).

of adequate quality are found. Pulse cycles that are interrupted by blinking or by saccadic eye movements can also be included in data evaluation; only the parts that lie between the first and the last visible fringes are then marked (e.g., see cycle 1 in Fig. 2, where fringe data is only available in parts 1 to 77). Averaging is performed by summing up the interpolated or marked interference orders for each of the 100 parts and dividing each part by the number of pulse periods that contributed to the sum of this specific part. In the example shown in Fig. 2, pulse cycles 1 and 3 contribute to the averaging of parts 1 to 77, e.g., the mean interference order of part 40 (indicated by red lines) is calculated by the interference orders from cycle 1 ($N = 3.25$) and cycle 3 ($N = 3.5$) as $N_{\text{mean},40} = (3.25 + 3.5)/2$. The mean interference order of part 90 (indicated by blue lines) is calculated in the same way from cycles 2 and 3. Missing data points at the beginning and at the end of pulse cycles are determined by linear interpolation of interference orders by using data, if available, from neighboring pulse periods.

Figure 3 shows the result of the averaging process of 14 pulse cycles, where the mean interference order is drawn as solid line, and the mean \pm standard deviation curves are shown as dashed lines. One can see that the peaks of the “mean + standard deviation” and the “mean – standard deviation” curves do not lie in the same part of the pulse cycle, i.e., there is a slight

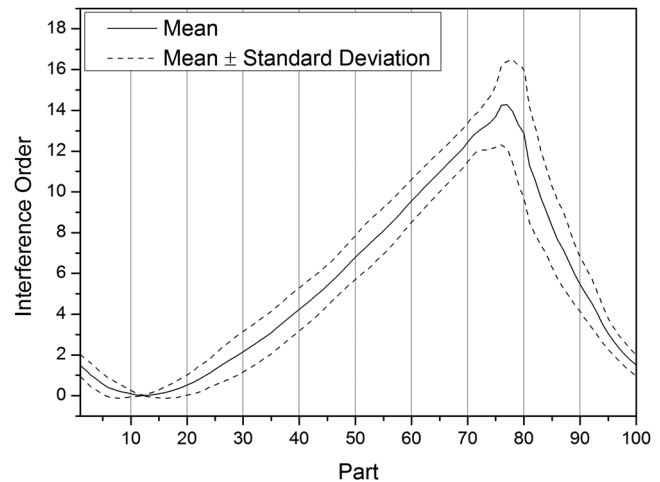


Fig. 3 Mean interference order (solid line) and mean \pm standard deviation (dashed lines) obtained by averaging interference orders from 14 pulse periods.

phase shift between these curves. Figure 3 allows estimation of how the results are influenced by fluctuations in interference order between pulse cycles. The maximum standard deviation in interference order is 3.20 (part 80 in the figure), resulting in a maximum standard deviation of $3.20 \times 0.84/2 = 1.34 \mu\text{m}$ in optical distance. The mean (averaged over the pulse cycle) standard deviation in interference order is 1.03, corresponding to $0.43 \mu\text{m}$ in optical distance.

Manually analyzing the synthetic interferograms makes the method quite time consuming. However, we believe that the described averaging algorithm allows for unbiased (robust to different users) assessment of the time course of ocular fundus pulsation, since it is simply based on counting and marking of interference fringes. Furthermore, any tendency to subjective bias can be avoided, e.g., by masking the test subject’s ID, angle to the vision axis, and axial position, before evaluating the data.

4 In Vivo Measurements

In vivo measurements were performed in the right eyes of three healthy emmetropic subjects at transversal angles from 0 deg to 18 deg in steps of 3 deg nasal to the axis of vision (in one subject at -3 deg to 18 deg). Smaller steps of 0.5 deg to 1 deg were chosen in the region of the ONH. For two subjects, a sagittal angle of 2 deg superior to the axis of vision was chosen to include the center of the ONH in the measurements. In one subject, the ONH center was found at a sagittal angle of 0 deg.

The fixation target (see Sec. 3.1) was moved horizontally and vertically by translation stages to set the transversal and sagittal angles. Gullstrand’s eye model was used to calculate the relation between the displacements of the fixation target and the viewing angles with respect to the axis of vision.

At each angle, at least three depth positions were selected for measurement. These correspond to the strongest reflecting structures that were found in the A-scan. The synthetic interferograms as well as the plethysmograms were recorded at these axial positions for 1 to 2 min to make sure that enough interference fringes with appropriate contrast were available for the described averaging algorithm. Between two recordings, several minutes’ break are required for the subject. Thus, about 25 to 30 min are needed for acquisition of three to

four depth positions at a certain horizontal angle. In our experience, after a maximum of 2 h, reliable fixation is not possible any more. This means that three to four transversal angles can be covered in one session. For this reason, measurement sessions had to be spread over several days. However, as described earlier, the averaging algorithm is robust to fluctuations of the pulse rate, so that the time courses obtained on different days are comparable.

5 Results

5.1 Topography

Optical distances between the anterior surface of the cornea and the structures in the fundus, as obtained with LCTI at transversal angles from 0 deg (in one subject from -3 deg) to 18 deg nasal to the axis of vision, are shown in Fig. 4. These distances—in the following referred to as depths—correspond to the positions of local maxima (peaks) in the respective A-scans. Fundus pulsations were evaluated, as described in Sec. 3.2, at all peak locations shown in Fig. 4.

The ONH can be identified in all subjects at transversal angles between 14 deg and 17 deg. The peaks corresponding to uppermost layers, i.e., shorter depth positions, at angles from 6 deg to 12 deg, most probably belong to the inner limiting membrane (ILM) and the retinal nerve fiber layer (RNFL). In subject 2, the measured depths decrease with increasing transversal angles; while in subject 3, there is a tendency of increasing depths with a marked drop at 18 deg. This observation can be attributed to the individual geometries, in particular retinal curvatures, of the eyes.

It is difficult to compare depths measured with LCTI with axial positions measured with spectral domain optical coherence tomography (SD-OCT). The dual-beam technique employed by LCTI requires alignment of the subject's eye, so that the reflection of the cornea has the same direction as the incident beam for achieving the necessary signal intensity. This means that for different angles to the axis of vision, the reference for length

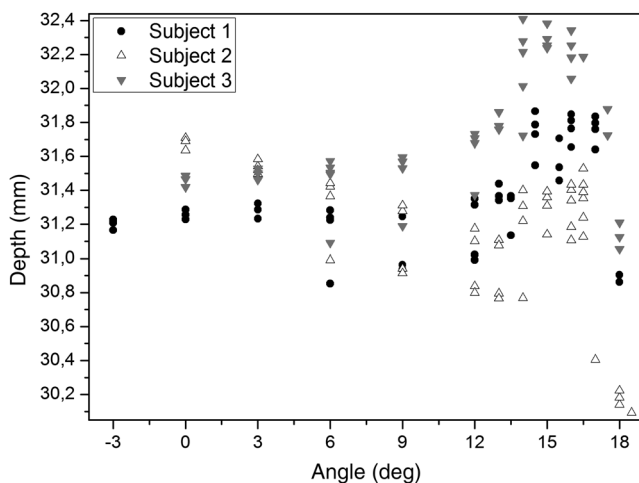


Fig. 4 Axial (depth) positions of A-scan peaks measured at transversal angles from 0 deg (-3 deg) to 18 deg nasal to the axis of vision. Peaks represent optical distances from the anterior surface of the cornea to the reflecting structures in the fundus that were selected for measurement of fundus pulsations. The optic nerve head (ONH) can be observed between 14 deg and 17 deg. At several angles (e.g., at 6 deg to 12 deg), the inner limiting membrane (ILM) can be identified as the innermost peak.

measurement lies at different points of the cornea. In SDOCT, the subject's eye is usually aligned in a way that the pivot point of the fast scanner is imaged onto the center of the pupil. This implies that in LCTI compared with SD-OCT, the measurement beams impinge at different points and at different angles onto the cornea and, thus, are not refracted in the same way by the optical system of the eye. The different ray paths encumber comparison of LCTI A-scans with SD-OCT tomograms. For this task, distortion correction of both measurement modalities in conjunction with extensive knowledge of the anatomy of the subject's eye would be required.²⁵

Although the optical path length in LCTI is influenced in a complex way by the geometry of the ocular surfaces and the distances between these surfaces, the optical path is predominantly determined by the geometry of the anterior corneal surface, as the refractive index change from air to cornea is the largest. Schmetterer et al. showed in a clinical study that accommodation of the lens has no significant influence on the measured FPA.⁷ This is in keeping with the following theoretical consideration. The FPA measured with LCTI is an optical distance and is converted to the geometrical FPA (FPAG) using the equation $FPAG = FPA/n_g(\text{eye})$, where $n_g(\text{eye})$ is the group refractive index of the eye. For the calculation of $n_g(\text{eye})$, the refractive indices of the cornea ($n_g = 1.3856$), the aqueous ($n_g = 1.3459$), the lens ($n_g = 1.4070$), and the vitreous ($n_g = 1.3445$) need to be known, together with the geometric parameters.¹¹ Using the paraxial schematic eye of Le Grand and El Hage,²⁶ with a corneal thickness of 0.55 mm, an anterior chamber depth of 3.05 mm, a lens thickness of 4 mm, and a vitreous chamber depth of 16.6 mm, the mean refractive index of the schematic eye can be calculated as $n_g(\text{eye}) = 1.3559$. Focusing the near point (i.e., full accommodation) increases lens thickness by about 200 μm and decreases the anterior chamber depth by the same value. This leads to a change in the group refractive index of the eye $n_g(\text{eye}) = 1.3564$. Consequently, the change in optical distance during accommodation leads to less than 1% change in FPAG, as calculated by the equation $FPAG = FPA/n_g(\text{eye})$, and is, therefore, negligible. Hence, it can strongly be assumed that the FPA measured through the cardiac cycle is caused by distance changes between the anterior surface of the cornea and the retina rather than by the accommodation or other changes in the optical pathway in the eye. Further, the points of incidence on the anterior cornea and on the retina stay (within certain limits given by the coherence length) the same during the measurement. Changes in these points would most likely lead to optical path lengths that do not match (within the coherence length) the eye length preselected by the interferometer arms, and thus, the interference pattern would not be visible. The fundus pulsation frequency is the same as that of the heart cycle, which also indicates that the measured FPA corresponds to the maximum distance change between the anterior surface of the cornea and the retina during the respective pulse period.

5.2 Amplitudes at Different Angles

In Fig. 5, the FPAs obtained at transversal viewing angles from 0 deg (in one subject from -3 deg) to 18 deg nasal to the axis of vision are shown. For each subject and at each angle, data points represent average FPAs from all measured depth positions. The solid line (mean, fit) was calculated by fourth-order polynomial fit to the average FPA from all subjects.

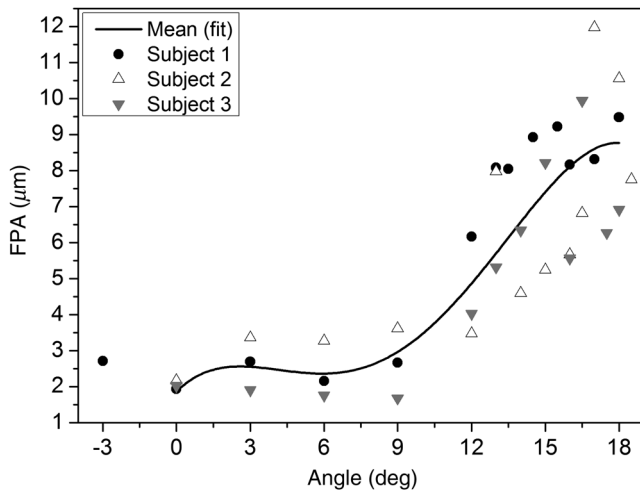


Fig. 5 Fundus pulsation amplitude (FPA) measured at transversal angles from 0 deg (–3 deg) to 18 deg nasal to the axis of vision. Data points represent average FPAs from all measured axial positions. Solid line (mean, fit) was calculated by a fourth-order polynomial fit.

As can be seen from Fig. 5, the FPAs in the ONH are about three times as high as in the macula. This can first be attributed to the fact that the large blood vessels with higher blood flow enter the eye in the ONH, and second to the differences in elastic properties between ONH and macula (see Sec. 6.1). The FPAs obtained with LCTI at different transversal angles are in good agreement with results from a previous study that show significantly higher FPAs in the optic disc than at other measurement sites.⁷ In this study, high within-subject variability was found for different measurement sites within the optic disc. A similar behavior was found in the current study, in particular in subjects 2 and 3, with considerable variations in FPA at transversal angles between 13 deg and 18 deg.

In Ref. 7, higher FPAs were found in the macula than at the surrounding measurement points; while in the current study, FPAs were higher at a transversal angle of 3 deg than in the macula. In this context, one should consider that the current study is based on measurements in three subjects, in contrast to 18 subjects in the study by Schmetterer et al.⁷

5.3 Time Courses

Figure 6 shows time courses of fundus pulsations measured in subject 1 at transversal angles from –3 deg to 18 deg nasal to the axis of vision. The time courses were reconstructed using the plethysmograms as time reference and the method described in Sec. 3.2. Similar to the FPAs discussed in Sec. 5.2, the curves depicted in Fig. 6 were—at each angle—obtained by averaging the displacements from all measured depth positions. Additionally, a sliding-window mean filter with window size 5 was applied to each curve.

In the retina at transversal angles smaller than 9 deg, the time courses exhibit a relatively short contraction phase (at 70% to 90% of the pulse cycle) followed by a long dilatation phase. As can be expected, the curves at –3 deg and 3 deg are quite similar. Interestingly, the curves at 0 deg and 6 deg are almost identical. Significantly different time courses are observed in the ONH and in its surroundings, where the curves are almost symmetrical, i.e., contraction and dilatation times are similar. The differences in the curves of ONH and retina become even

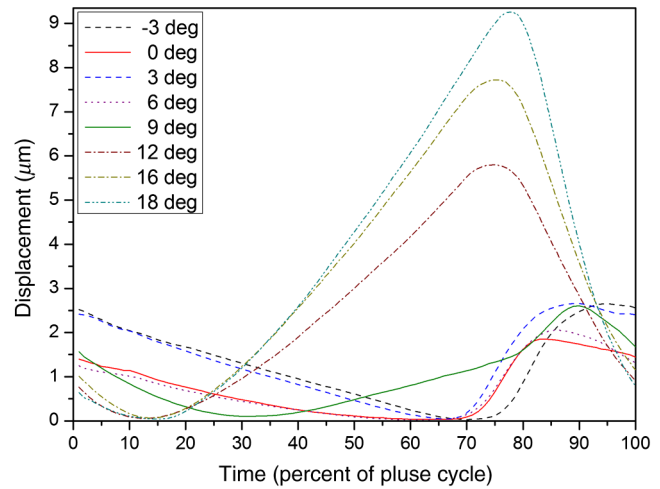


Fig. 6 Time courses of fundus pulsations measured at transversal angles from –3 deg to 18 deg nasal to the axis of vision in subject 1. Displacements at all measured axial positions were averaged. A sliding-window mean filter with window size 5 was applied to each curve. Two distinctly different shapes of time courses belonging to the retina and the ONH are found.

more obvious when looking at the points of minimum displacement, which lie at approximately 15% of the pulse period for curves that were obtained in the ONH and at 65% for retinal curves. At a transversal angle of 9 deg, a transition zone exists with a time course that comes close to that of the ONH, but with an amplitude similar to amplitudes found at smaller angles. Most probably, the observed differences in the time courses of ONH and retina are due to differences in blood flow and vasculature (vessel size and ratio of arteries to veins) as well as in biomechanical properties. An impression of the actual movement of the tissue structures during the heart cycle based on the time courses of a large number of measurement points is given by fundus pulsation movies (see Sec. 5.5).

5.4 Depth Dependency in the ONH

FPAs were measured in subjects 1 to 3 at angles nasal to the axis of vision ranging from 0 deg (–3 deg) to 18 deg and in selected depths corresponding to the reflecting structures in the fundus. Thus, data points are three-dimensional (FPA, angle, and depth). Whereas depth versus angle and FPA versus angle have been presented in Figs. 4 and 5, respectively, Figure 7 gives an overview of the FPAs measured in different depths. In subjects 1 and 3, the FPAs can roughly be divided into two groups belonging to the retina (shallower depths) and the ONH (greater depths). However, some data points in these subjects show high FPAs at relatively shallow depths, which correspond to the measurements at large transversal angles after the center of the ONH. In subject 2, no such groups can be found, which is due to the decrease in axial length with increasing angle. Plotting FPAs in different depths, as shown in Fig. 7, however, does not allow for the interpretation of results with respect to the differences in FPA found in different axial positions within the same region, e.g., the retina or the ONH. An approach to compare FPAs measured in different axial depths within the ONH is described here.

According to the predictions from generic and eye-specific biomechanical models, the displacements of the ONH surface and the lamina cribrosa (LC), during an increase in IOP, are

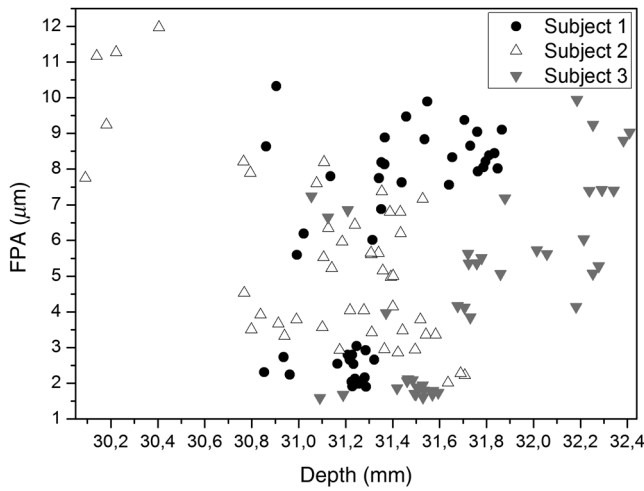


Fig. 7 FPA measured at selected axial positions corresponding to the reflecting structures in the fundus at transversal angles from 0 deg (-3 deg) to 18 deg nasal to the axis of vision. In subjects 1 and 3, the FPAs can roughly be divided into two groups belonging to the retina and the ONH, while in subject 2, due to the decrease in axial length with increasing angle, no such groups can be found.

not identical.^{19,21-23} To evaluate whether FPAs in different depths within the ONH measured with LCTI are different, the measured FPAs were grouped according to the depth of the measured structure into inner, intermediate, and outer regions (see Fig. 8). The intermediate depth range was selected to cover a distance of 0.2 mm in all subjects and was arranged for each subject, so that at least three data points lie within each region. The FPAs within each distance range are shown in Fig. 9. Box-whisker plots indicate the median (line) and the mean (small box) values, the 25% and 75% quartiles, as well as the minimum and maximum values lying within 1.5× interquartile range. In subjects 1 and 3, the FPAs in the inner measurement sites appear to differ from FPAs in the intermediate and the outer depth ranges.

One drawback of this representation of FPA depth-dependency comes from the fact that the FPA also changes with transversal angle (see Fig. 5). Since the numbers of measurement

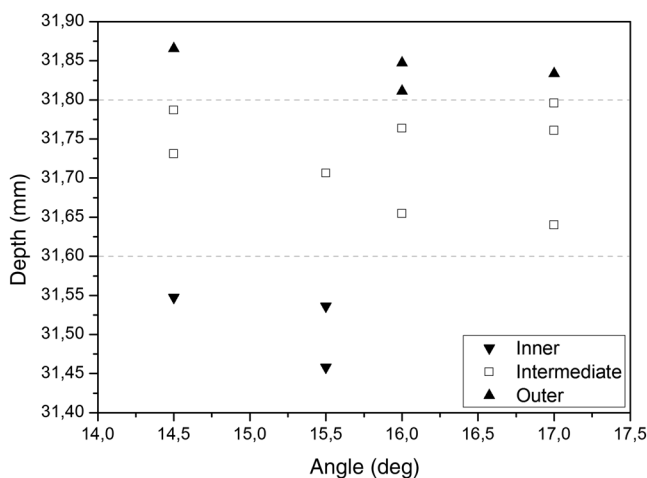


Fig. 8 Grouping of measurement sites according to inner, intermediate, and outer depth ranges in the ONH of subject 1. The intermediate depth range covers a distance of 0.2 mm and is arranged, so that each group consists of at least three data points.

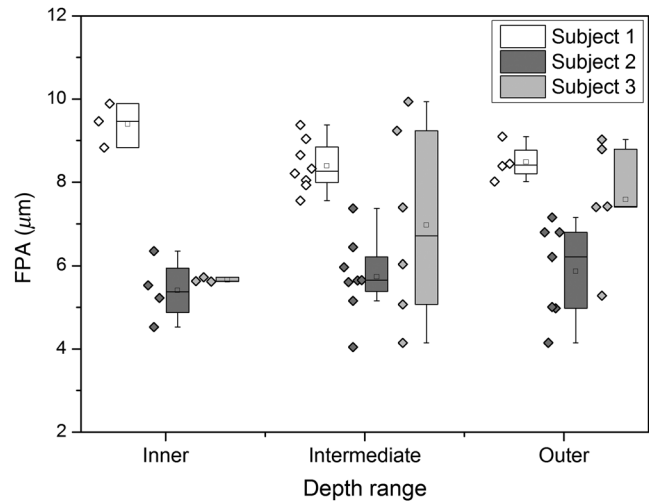


Fig. 9 FPAs in the inner, intermediate, and outer depth ranges. Box-whisker plots indicate the median (line) and mean (small box) values, the 25% and 75% quartiles, as well as the minimum and maximum values lying within 1.5× interquartile range. In subjects 1 and 3, the FPAs in inner measurement sites appear to differ from FPAs in intermediate and outer depth ranges.

sites belonging to the inner, intermediate, and outer depth ranges are not the same at each angle, the calculated average can be biased toward measurement sites that lie at angles within high FPA. A possible solution to this problem is to scale the FPAs at each angle, so that in the intermediate region the average FPA is 1 (arbitrary units). In the current study, this can be done because intermediate data points are present in all subjects and at all angles. The scaled FPAs (data points beside box-whisker plots) are shown in Fig. 10. Please note that the distribution of FPAs is changed by scaling, since the scaling factors vary for measurement sites in the same region but at different angles. In subjects 1 and 3, there is a tendency to lower FPAs in the intermediate region compared with the outer region, while in subject 2, the FPAs in the inner and the outer regions seem to be lower than in the intermediate range. However, these

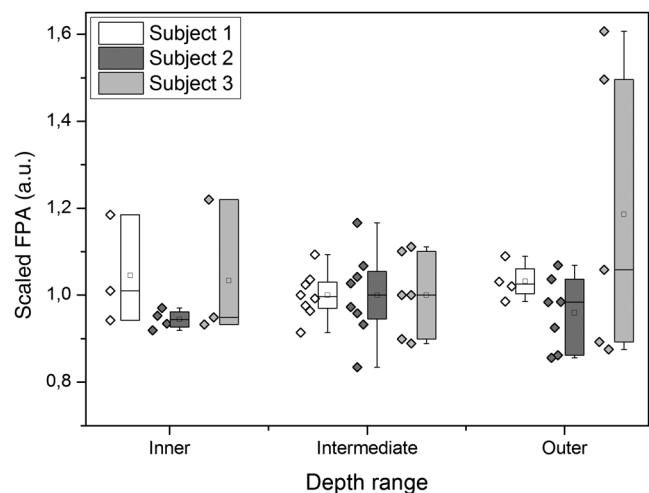


Fig. 10 FPAs are scaled, so that the average FPA in the intermediate region at each transversal angle is 1 (in arbitrary units). Box-whisker plots indicate the median (line) and mean (small box) values, the 25% and 75% quartiles, as well as the minimum and maximum values lying within 1.5× interquartile range.

differences do not reach statistical significance. Studies of a larger number of subjects are required to gain deeper insight into the axial and lateral distributions of FPAs.

5.5 Fundus Pulsation Movies

Time courses for all measurement sites shown in Fig. 4 were reconstructed using the method described in Sec. 3.2. Diagrams showing the actual depth of each reflecting structure, i.e., the sum of the optical distance from the cornea and the displacement obtained by the synthetic interferogram, were created for each of the 100 parts of the pulse cycle. For better visibility, the pulse-related movement was exaggerated by a factor 10. The diagrams were assembled to fundus pulsation movies (see Videos 1, 2, and 3) with a frame rate of 60 frames/s, i.e., one pulse period covers 1.67 s. One has to note that the magnification of the displacement leads to unrealistic distance changes between the measured points, i.e., structures in the movies come much closer than they would in reality. Further, magnification of the movement exaggerates the phase differences that occur due to the limited number of pulse cycles included in the averaging process. Magnification, however, is necessary, since the FPA (several micrometers) is much smaller than the distances between the measured layers (1.4 to 2 mm in the current movies).

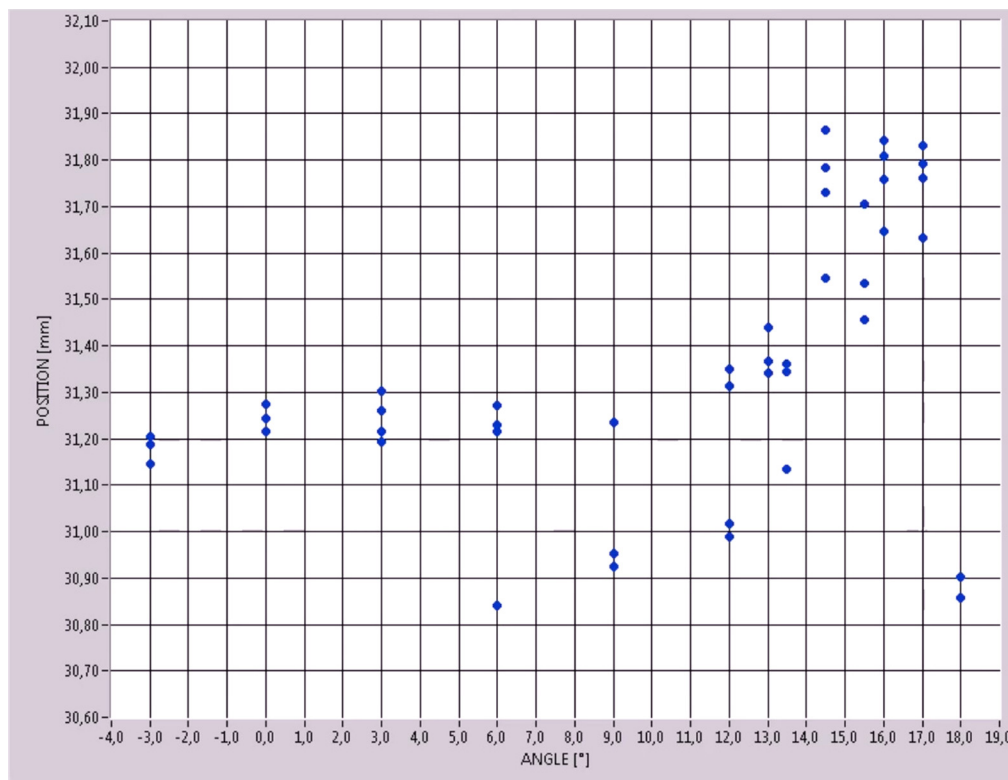
At small angles to the vision axis, reflections from the ILM and the RNFL are very weak and are not observable with LCTI. At angles of 6 deg and larger, in the LCTI depth scans, these inner structures (ILM and RNFL) can be observed, and the movement of these structures can be assessed, as shown in the fundus pulsation movies.

6 Discussion

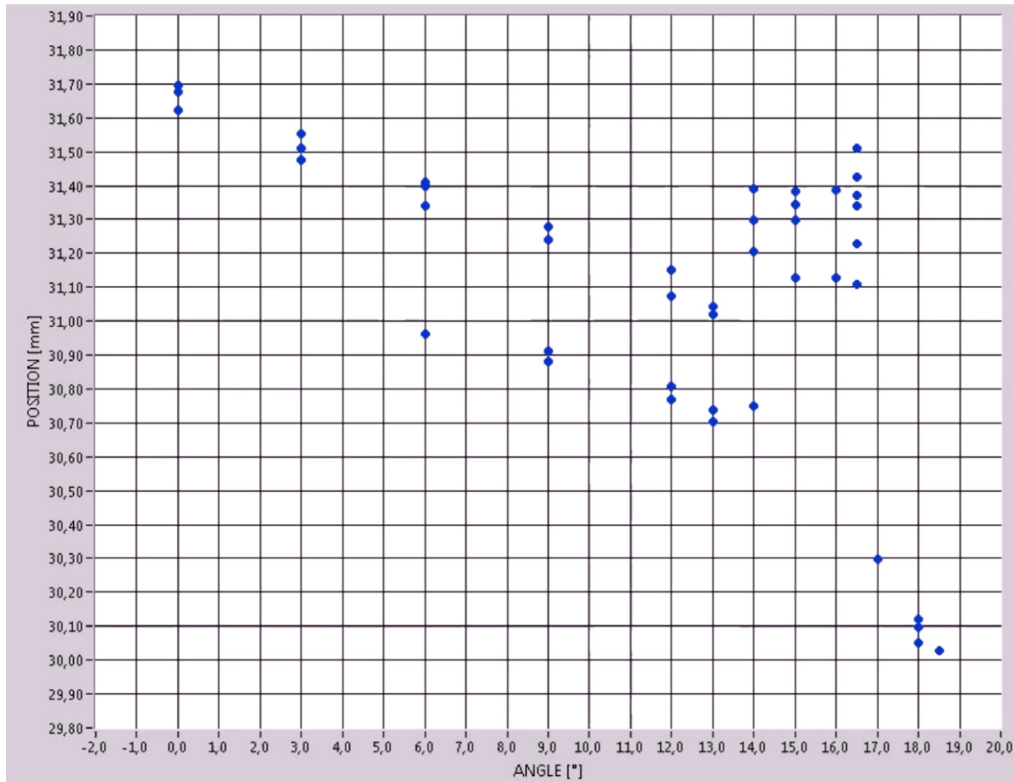
6.1 Biomechanical Models

Biomechanical properties of the sclera, the ONH, and, in particular, of the LC are hypothesized to play a role in retinal ganglion cell loss and in tissue remodeling in glaucoma. The disease is often, but not always, associated with increased IOP. Several models of ONH and LC biomechanics have been proposed with the aim of understanding how mechanical changes are transformed into a biological response of the tissue.²⁷ Numerical models based on finite-element modeling allow for calculating deformations of ONH and LC tissues at different levels of IOP.¹⁸⁻²⁴ These models are classified as generic and eye-specific models. Generic models are usually developed from population-based dimensions and material properties, while eye-specific models contain more details of an individual eye, often obtained by imaging histological sections of postmortem eyes. Sigal et al. developed a generic model of the ONH incorporating pre- and post-laminar neural tissues, which allows comparison of IOP-induced displacements of the ONH surface with those of the LC. They found that these displacements, while related, are far from identical.¹⁹ The results were confirmed in a later study using eye-specific models.²¹⁻²³

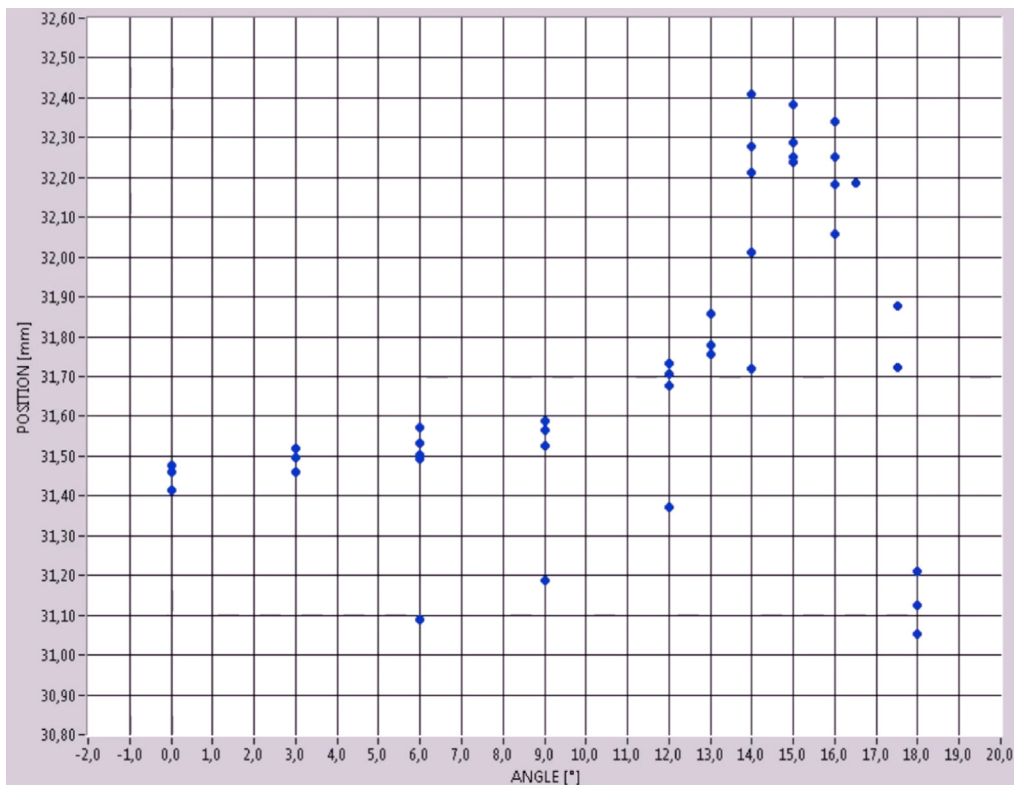
Current models of ONH biomechanics are based on *in vitro* measurements of biomechanical properties as well as *ex vivo* measurements of individual ONH geometries. Since the LC is difficult to access, in several studies, the movement of the vitreoretinal interface of the ONH has been used as surrogate for displacement of the LC.^{28,29} However, as mentioned earlier, this might be problematic, because the displacements of the ONH surface and the LC are most probably not identical.



Video 1 Fundus pulsation movie recorded from subject 1 at transversal angles from -3 deg to 18 deg nasal to the vision axis (MOV, 791 KB) [URL: <http://dx.doi.org/10.1117/1.JBO.18.12.121502.1>].



Video 2 Fundus pulsation movie recorded from subject 2 at transversal angles from 0 deg to 18.5 deg nasal to the vision axis (MOV, 652 KB) [URL: <http://dx.doi.org/10.1117/1.JBO.18.12.121502.2>].



Video 3 Fundus pulsation movie recorded from subject 3 at transversal angles from 0 deg to 18 deg nasal to the vision axis (MOV, 618 KB) [URL: <http://dx.doi.org/10.1117/1.JBO.18.12.121502.3>].

Deformation of the LC has been measured *ex vivo* using radiographic³⁰ and histologic^{17,31} methods. In a study in monkey eyes, evidence for remodeling of the LC and the peripapillary sclera were found using an early glaucoma model of induced ocular hypertension.¹⁷ However, data on displacement of structures within the ONH obtained from *in vivo* measurements are required for verification and refinement of biomechanical models. Although the LC could not be directly identified in our measurements, we were able to measure displacements in the ONH in different depths and transversal positions. Thus, we believe that LCTI can yield important data for the further development of biomechanical models of the ONH. It may also contribute to predict an individual's susceptibility to elevated IOP, which is hypothesized to be closely related to ocular rigidity (stiffness).¹⁶

One approach to estimate ocular rigidity E *in vivo* is based on the Friedenwald equation,³²

$$E = \left[\frac{(\log IOP_1 - \log IOP_2)}{\Delta V} \right],$$

where IOP_2 and IOP_1 are the highest IOP during systole and the lowest IOP during diastole, respectively, and ΔV is the change in ocular volume during the cardiac cycle. In this equation, E describes the combined structural stiffness of all ocular components. When E increases, the eye is stiffer, and when E decreases, the eye is less stiff. In a study of patients with primary open-angle glaucoma, Hommer et al. measured pulse-related changes in IOP using pneumotometry and FPA using a laser beam of long coherence length.¹⁶ They assumed that the ocular volume change ΔV can be estimated based on measurement of FPA. Assuming that ΔV is proportional to FPA, they calculated a factor $E_1 = (\log IOP_1 - \log IOP_2)/FPA$ related to ocular rigidity as obtained by the Friedenwald equation. The factor E_1 was found to be significantly higher in glaucoma patients compared with the healthy control group.¹⁶ Whether increased ocular stiffness is a primary factor contributing to the development of glaucoma or a secondary effect of the disease still has to be clarified in future studies. Hommer et al. chose the macula as the location for measurement of FPA. They considered E_1 as combined factor of stiffness of all ocular components including sclera, choroid, Bruch's membrane, retina, and cornea. However, the FPA at a certain transversal and axial location depends on the change in intraocular volume due to blood flow as well as on local material properties. Thus, LCTI could become a tool for *in vivo* estimation of (local) ocular rigidity, due to its ability of measuring the FPA in selected depths and fundus locations.

6.2 Measurement of Fundus Pulsation with SD-OCT

An SD-OCT system for assessment of ocular fundus pulsations based on the simultaneous measurement of pulse-related axial movements of cornea and retina has recently been presented by Singh et al.³³⁻³⁶ They found that in young healthy subjects, the amplitudes of corneal and retinal movements are almost equal (28 ± 9 and $29 \pm 9 \mu\text{m}$, respectively), and that there is a phase shift between these movements ranging from 1 deg to 20 deg. Furthermore, Singh et al. found harmonics by frequency analysis in addition to the fundamental frequency of the heartbeat in the movement of cornea and retina as well as in the time course of the distance change between these two surfaces. They hypothesized that the measured FPA

($4 \pm 2 \mu\text{m}$) is mainly due to the phase shifts between the movement of cornea and retina.

Contrary to LCTI, the system presented in Ref. 34 is able to determine the displacement of each ocular component separately. However, the signal obtained by SD-OCT is strongly influenced by axial head movements. To overcome this problem, Singh et al. performed postprocessing of the distance change between cornea and retina by bandpass frequency filtering between the heartbeat frequency and its fifth harmonic. By this method, more or less irregular time courses of fundus pulsations were found. This is in contrast to the time courses observed in LCTI, where regular, periodic time courses are observed. Singh et al. claim that the predominant frequency components in the FPA time courses are the (fundamental) heartbeat frequency and its second harmonic,³⁴ while the time courses found in our study are strongly dominated by the heartbeat frequency (see Fig. 6). Other frequency components were not observed in the current study. When comparing the results from SD-OCT and LCTI, one has to keep in mind that LCTI directly measures the distance change between the cornea and the selected structure in the fundus, while the SD-OCT signal is influenced by axial head movements, which have usually much larger amplitudes than the FPA. Consequently, a bandpass filter has to be applied to the time courses obtained in SD-OCT. As such, it is unclear whether the described filtering process is responsible for the behavior of the fundus pulsation time course found by Singh et al.

7 Conclusion

LCTI enables depth-resolved measurement of FPAs and, by coupling the device with a pulse oximeter, reconstruction of time courses of the movement of ocular structures relative to the cornea in preselected depths and fundus locations. We have shown that the time courses and amplitudes of ocular fundus pulsations in the retina and the ONH are significantly different. Further studies are required to investigate whether the FPAs within the ONH depend on the axial position (depth), as has been predicted by several biomechanical models. We have further presented fundus pulsation movies corresponding to the time courses found in three healthy young subjects at different axial and lateral positions including macula and ONH.

The long measurement times and the necessity for manually marking the interference fringes make LCTI currently not suitable for application in large-scale clinical studies. However, the method offers several advantages over other presented methods (SD-OCT), since it makes the distance change between the cornea and the selected structure in the fundus directly accessible, without the need for further filtering.

Present day numerical models of the ONH are based on *ex vivo* and *in vitro* experiments, which cannot provide comprehensive insight into the behavior of living tissue. LCTI allows for measuring the local fundus pulsation resulting from volume changes caused by imbalances of inflow and outflow during the cardiac cycle. The FPA depends on the volume change as well as on the local tissue properties of the eye. Thus, we believe that LCTI can provide important information on local tissue properties of an individual eye.

References

- O. Findl et al., "Assessment of optic disk blood flow in patients with open-angle glaucoma," *Am. J. Ophthalmol.* **130**(5), 589-596 (2000).

2. L. Schmetterer et al., "Topical fundus pulsation measurements in age-related macular degeneration," *Graefes Arch. Clin. Exp. Ophthalmol.* **236**(3), 160–163 (1998).
3. L. Schmetterer and M. Wolzt, "Ocular blood flow and associated functional deviations in diabetic retinopathy," *Diabetologia* **42**(4), 387–405 (1999).
4. K. Polak et al., "Choroidal blood flow and arterial blood pressure," *Eye* **17**(1), 84–88 (2003).
5. L. Schmetterer and M. Wolzt, "Laser interferometric investigations of pulsatile choroidal blood flow: review and new results on the validity of the technique," *J. Biomed. Opt.* **3**(3), 246–252 (1998).
6. L. Schmetterer and G. Garhöfer, "How can blood flow be measured?," *Surv. Ophthalmol.* **52**(6), S134–S138 (2007).
7. L. Schmetterer et al., "A comparison between laser interferometric measurement of fundus pulsation and pneumotonometric measurement of pulsatile ocular blood flow. 1. Baseline considerations," *Eye* **14**(Pt 1), 39–45 (2000).
8. L. Schmetterer et al., "A comparison between laser interferometric measurement of fundus pulsation and pneumotonometric measurement of pulsatile ocular blood flow. 2. Effects of changes in pCO₂ and pO₂ and of isoproterenol," *Eye* **14**(Pt 1), 46–52 (2000).
9. L. Schmetterer et al., "Topical measurement of fundus pulsations," *Opt. Eng.* **34**(3), 711–716 (1995).
10. N. Dragostinoff et al., "Depth-resolved measurement of ocular fundus pulsations by low-coherence tissue interferometry," *J. Biomed. Opt.* **14**(5), 054047 (2009).
11. C. K. Hitztenberger, "Optical measurement of the axial eye length by laser Doppler interferometry," *Invest. Ophthalmol. Visual Sci.* **32**(3), 616–624 (1991).
12. C. K. Hitztenberger, "Measurement of corneal thickness by low-coherence interferometry," *Appl. Opt.* **31**(31), 6637–6642 (1992).
13. G. Fuchsjaeger-Mayrl et al., "Ocular blood flow and systemic blood pressure in patients with primary open angle glaucoma and ocular hypertension," *Invest. Ophthalmol. Visual Sci.* **45**(3), 834–839 (2004).
14. M. Mozaffarieh, M. C. Grieshaber, and J. Flammer, "Oxygen and blood flow: players in the pathogenesis of glaucoma," *Mol. Vis.* **14**, 224–233 (2008).
15. H. Resch et al., "Endothelial dysfunction in glaucoma," *Acta Ophthalmol.* **87**(1), 4–12 (2009).
16. A. Hommer et al., "Estimation of ocular rigidity based on measurement of pulse amplitude using pneumotonometry and fundus pulse using laser interferometry in glaucoma," *Invest. Ophthalmol. Visual Sci.* **49**(9), 4046–4050 (2008).
17. J. C. Downs et al., "Three-dimensional histomorphometry of the normal and early glaucomatous monkey optic nerve head: neural canal and subarachnoid space architecture," *Invest. Ophthalmol. Visual Sci.* **48**(7), 3195–3208 (2007).
18. A. J. Bellezza, R. T. Hart, and C. F. Burgoyne, "The optic nerve head as a biomechanical structure: initial finite element modeling," *Invest. Ophthalmol. Visual Sci.* **41**(10), 2991–3000 (2000).
19. I. A. Sigal et al., "Finite element modeling of optic nerve head biomechanics," *Invest. Ophthalmol. Visual Sci.* **45**(12), 4378–4387 (2004).
20. I. A. Sigal, J. G. Flanagan, and C. R. Ethier, "Factors influencing optic nerve head biomechanics," *Invest. Ophthalmol. Visual Sci.* **46**(11), 4189–4199 (2005).
21. I. A. Sigal et al., "Predicted extension, compression and shearing of optic nerve head tissues," *Exp. Eye Res.* **85**(3), 312–322 (2007).
22. I. A. Sigal et al., "Modeling individual-specific human optic nerve head biomechanics. Part I: IOP-induced deformations and influence of geometry," *Biomech. Model. Mechanobiol.* **8**(2), 85–98 (2009).
23. I. A. Sigal et al., "Modeling individual-specific human optic nerve head biomechanics. Part II: influence of material properties," *Biomech. Model. Mechanobiol.* **8**(2), 99–109 (2009).
24. I. A. Sigal and C. R. Ethier, "Biomechanics of the optic nerve head," *Exp. Eye Res.* **88**(4), 799–807 (2009).
25. S. Ortiz et al., "Optical distortion correction in optical coherence tomography for quantitative ocular anterior segment by three-dimensional imaging," *Opt. Express* **18**(3), 2782–2796 (2010).
26. Y. Le Grand and S. G. El Hage, *Physiological Optics*, Springer, Berlin (1980).
27. C. F. Burgoyne et al., "The optic nerve head as a biomechanical structure: a new paradigm for understanding the role of IOP-related stress and strain in the pathophysiology of glaucomatous optic nerve head damage," *Prog. Retinal Eye Res.* **24**(1), 39–73 (2005).
28. R. C. Zeimer and K. Chen, "Comparison of a noninvasive measurement of optic nervehead mechanical compliance with an invasive method," *Invest. Ophthalmol. Visual Sci.* **28**(10), 1735–1739 (1987).
29. A. P. Wells et al., "Corneal hysteresis but not corneal thickness correlates with optic nerve surface compliance in glaucoma patients," *Invest. Ophthalmol. Visual Sci.* **49**(8), 3262–3268 (2008).
30. N. S. Levy and E. E. Crapps, "Displacement of optic nerve head in response to short-term intraocular pressure elevation in human eyes," *Arch. Ophthalmol.* **102**(5), 782–786 (1984).
31. J. B. Jonas, E. Berenshtein, and L. Holbach, "Lamina cribrosa thickness and spatial relationships between intraocular space and cerebrospinal fluid space in highly myopic eyes," *Invest. Ophthalmol. Visual Sci.* **45**(8), 2660–2665 (2004).
32. J. S. Friedenwald, "Contribution to the theory and practice of tonometry," *Am. J. Ophthalmol.* **20**, 985–1024 (1937).
33. K. Singh et al., "Development of a novel instrument to measure the pulsatile movement of ocular tissues," *Exp. Eye Res.* **91**(1), 63–68 (2010).
34. K. Singh et al., "Measurement of ocular fundus pulsation in healthy subjects using a novel Fourier-domain optical coherence tomography," *Invest. Ophthalmol. Visual Sci.* **52**(12), 8927–8932 (2011).
35. K. Singh et al., "Pulsatile movement of the optic nerve head and the peripapillary retina in normal subjects and in glaucoma," *Invest. Ophthalmol. Visual Sci.* **53**(12), 7819–7824 (2012).
36. C. Dion et al., "Analysis of pulsatile retinal movements by spectral-domain low-coherence interferometry: influence of age and glaucoma on the pulse wave," *PLoS One* **8**(1), e54207 (2013).